Journal of Applied Fluid Mechanics, Vol. 16, No. 10, pp. 1962-1973, 2023.
Available online at www.jafmonline.net, ISSN 1735-3572, EISSN 1735-3645.
https://doi.org/10.47176/jafm.16.10.1919

Ballistic Characteristics of High-Speed Projectiles Entering Water Vertically

B. Hao[1,2], Y. G. Lu[1†] and H. Dai[1]

[1] *School of Mechanical Engineering and Automation, Northeastern University, Shenyang110819, China*
[2] *School of Control Engineering, Northeastern University at Qinhuangdao, Shenyang Qinhuangdao 066004, China*

†*Corresponding Author Email: luyuangen97@163.com*

ABSTRACT

The formation of supercavitation after a high-speed projectile enters water has a decisive impact on the underwater ballistic and penetration of the projectile. In this study, Ansysfluent19.0 simulation software is used to study water entry of a chosen projectile at velocities of 300, 400, 500, and 600 m/s. The underwater cavitation characteristics, trajectories, and flow-field characteristics are analyzed for a 5.8-mm caliber conical flat head projectile, as well as for t wo other projectiles of the same caliber and different head shapes — conical cone head and elliptical flat head — entering water vertically at the same velocities. The attenuation rate of water entry velocity increases with the increase of velocity. Within first 3ms, the velocity attenuation rate of the conical flat-head projectile with a water entry velocity of 600m / s is 55.6 %, while the velocity attenuation rate of the projectile with a water entry velocity of 300m / s is only 16.3 % within 3ms. Among the head shapes considered, the conical flat head projectile is the most stable for vertical water entry. The stability of an elliptical flat head projectile is worse, and the trajectory stability of a conical cone head projectile is still worse.

Article History

Received April 6, 2023
Revised June 16, 2023
Accepted June 19, 2023
Available online July 29, 2023

Keywords:

Water-entry velocity, Supercavitation
Cavity shape
High- speed projectile
Multiphase flow

1. INTRODUCTION

The cavitation phenomenon of an object entering water is an interesting topic worthy of study. In the 20th century, researchers worked on related issues. Miloh (1981, 1991a, 1991b) experimentally studied the load and flow distribution of inclined and vertical water entry of a sphere, and proposed a number order expression of the drag coefficient and the slam load of at the moment the ball enters the water. Lee et al. (1997) studied the water entry characteristics of a sphere at different speeds, ignoring the viscosity of the fluid.When the velocity is small, the cavity closure will occur after the surface closure. In recent years, cavitation phenomenon and ballistic stability of a projectile entering water have attracted the interest of many researchers and have been explored through numerical simulation. Based on the Navier-Stokes (N-S) equation and the fluid volume multiphase flow (VOF) model, Wang (2019) carried out a numerical simulation for a spherical projectile, and analyzed the influence of surface roughness of the projectile on its hydrodynamic characteristics. Xiao et al. (2019) used six-degrees-of-freedom (6DOF) and overlapping networks to find the properties of projectiles entring water at small angles and analyzed the angle-dependence of the ballistic characteristics of such projectiles. Their results show that in the early stage of a projectile contacts with the water, the trajectory is approximately a straight line. But after a period of time, the trajectory of the projectile is strongly deflected by the flow force generated by the contact between the lower surface of the projectile and the water. Huang (2018) used dynamic network technology combined with the 6DOF control equation to carry out numerical simulation studies of a projectile of 12.7-mm caliber. Smirnov et al. (2020, 2022) presented a new algorithm and studied the problem of hypervelocity impact of projectiles with different configurations and different materials. These results showed that the stability of the underwater projectile is related to its angle of entry, initial velocity, and rotational speed. Therefore, it is important to learn about the rules governing the underwater behavior of high-speed projectiles at different initial speeds to further improve understanding of their underwater ballistic characteristics.

Some progress has been made in the study of projectile water entry characteristics based on factors such as velocity and head shape. Guo et al. (2012) analyzed the resistance coefficient of projectiles with different velocities and shapes, and found that projectiles

NOMENCLATURE

A_0	projectile maximum cross-sectional area	x	distance in the x direction
C_d	drag coefficient	x_i	the corresponding coordinate.
C_l	lift coefficient	y	minimum distance between node and wall
$CD_{k_{tke}\omega}$	cross-diffusion	α	volume fraction of water vapor phase
Courant	constants	α_c	projectile velocity attenuation coefficient
F_{va} F_{con}	empirical constants	α_{ncg}	volume fraction of non-coagulate gas
F_b	the specific expression for the mixing function	$\beta_w\beta_v\beta_a$	the volume fractions of water, air, and water vapor phases
F_d	drag force acting on projectile head	$\beta^{'}$、β	constants
F_l	lift force acting on projectile head	σ_k、σ_ω	constants
F_s	lateral force acting on projectile head	μ	dynamic viscosity of fluid
G	transform matrix	μ_m	dynamic viscosity of mixture
k_{tke}	turbulent kinetic energy	μ_t	coefficient of eddy viscosity
m_p	projectile mass	ρ_m	fluid mixture density
N	number of bubbles per unit volume	ρ_v ρw	the densities of water vapor and water
P	turbulent kinetic energy term caused by velocity gradient	ρ	projectile density
P_{kb} $P_{\omega b}$	turbulent kinetic energy terms caused by buoyancy	ω	turbulence frequency
R_B	bubble radius	$\overrightarrow{v_{c,g}}$	linear velocity of the projectile
R_{B2}	gas nucleus radial reference from the Rayleigh formula	$\overrightarrow{\omega_{c,g}}$	angular velocity
S	invariant measure of shear strain rate	$\overrightarrow{\theta_{c,g}^n}$	calculation step *n* in the projectile's direction of motion
u_i	component of fluid velocity in the i direction	$\overrightarrow{x_{c,g}^n}$	position of the projectile's center of mass at the *n*th calculation step
v	kinematic viscosity	Δx	overall length of projectile
v_p	linear velocity of projectile		

of different velocities had basically the same cavity size before a deep pinch phenomenon occurred. Guo et al. (2020) studied the cavitation characteristics and velocity attenuation law of a series of projectiles with different velocities in a closed container, and found a basic law relating velocity attenuation and container size. Using Fluent fluid calculation software as a platform, Meng et al. (2019) found the relevant characteristics of projectiles entering the water vertically, and studied the rules governing cavitation closure of a projectile which velocity is subsonic velocity. They found that when the velocity of the projectile approached the speed of sound in the water, a bow shock wave was generated when the projectile head entered the water. Chen et al. (2021), through experiments on projectiles of different shapes entering the water at different speeds, found that increasing the velocity can accelerate the development of cavitation and improve the stability of projectiles motion. Fan (2022) numerically studied the resistance characteristics and flow characteristics of projectiles with free and constant velocity entering water. It was found that the resistance characteristics are mainly related to the head shape and the velocity of the projectile. However, these studies were not comprehensive enough to reveal the ballistic characteristics of high-speed projectiles entering water vertically. In order to further study the influence of water-entry velocity on the underwater stability of ballistics, this study comprehensively analyzes the cavitation shape, and resistance coefficient of projectiles with different water-entry velocities through numerical simulation. The influence pattern of projectile head shape and velocity on projectile cavitation and ballistic stability.is found, and provides a reference for studying the stable behavior of projectiles with higher penetration ability.

At present, research on supercavitating weapons is active, and many researchers have studied the problem of water entry. However, study of the cavitation and ballistic characteristics of underwater projectiles is not yet thorough enough. In order to better understand the effects of velocity and underwater pressure on projectiles, this study simulates vertical water entry with initial velocities of 300, 400, 500, and 600 m/s. In this study, VOF and turbulence models are adopted on the Reynolds mean-time N-S equation. The Schnerr-Saer cavity model combines the 6DOF dynamic network technology and analyzes the

effect of inlet velocity on cavity, trajectory, and flow field characteristics. The results of this study can promote understanding of the way that cavitation influences the steadiness of the underwater trajectory of the projectile. This analysis shows that the best shape of the projectile is a conical flat head. Finally, the ballistic stability of different projectiles with conical flat head, conical cone head, and elliptical flat head is studied.

2. NUMERICAL CALCULATION MODEL

2.1 Basic Control Equation

2.1.1 VOF Model

In the numerical simulation carried out in this paper, the VOF model is used to describe the multiphase flow formed by air, water, and water vapor generated by friction between the projectile and water when a projectile enters the water. Volume fractions are introduced to describe the proportion of different phases in the fluid medium — β_w, β_v, and β_a are the volume fractions of water, water vapor, and air, respectively, and satisfy Eq. (1) in all computational domains of the flow field:

$$\beta_w + \beta_v + \beta_a = 1 \tag{1}$$

Eq (2) is the continuity equation of the fluid mixture:

$$\frac{\partial \rho_m}{\partial t} + \frac{\partial}{\partial x_i}(\rho_m u_i) = 0 \tag{2}$$

In this equation，$i = 1$，2，3; u_i is the component of the fluid velocity in the i direction; and x_i is the corresponding coordinate.

The momentum conservation equation of fluid mixing is Eq. (3):

$$\begin{aligned}&\frac{\partial}{\partial t}(\rho_m u_i) + \frac{\partial}{\partial x_j}(\rho_m u_i u_j) = -\frac{\partial p}{\partial x_i} \\ &+ \frac{\partial}{\partial x_i}[(\mu_m + \mu_t)(\frac{\partial u_i}{\partial x_j} + \frac{\partial u_j}{\partial x_i})]\end{aligned} \tag{3}$$

where μ_m is the dynamic viscosity, given by $\mu_m = \beta_w\mu_w + \beta_v\mu_v + \beta_a\mu_a$; μ_t is the turbulent viscosity coefficient; X is distance in the X direction; and ρ_m is the density of the fluid.

2.1.2 SST k-ω Turbulent Flow Model

The SST k-ω turbulent flow model can solve the flow separation problem and achieve good accuracy of the cavitation characteristic when a high-speed projectile enters water. Its mathematical expression may be written

$$\begin{aligned}&\frac{\partial(\rho k)}{\partial t} + \frac{\partial(\rho u_j k)}{\partial x_j} = \\ &+ \frac{\partial}{\partial x_j}[(\mu + \sigma_k\mu_t)\frac{\partial k}{\partial x_j}] - \beta^{'}\rho\omega k + P + P_{kb}\end{aligned} \tag{4}$$

$$\begin{aligned}&\frac{\partial(\rho\omega)}{\partial t} + \frac{\partial(\rho u_j \omega)}{\partial x_j} = \frac{\partial}{\partial x_j}[(\mu + \sigma_\omega\mu_t)\frac{\partial \omega}{\partial x_j}] + P_{\omega b} \\ &+ \alpha\frac{\omega}{k_{tke}}P - \beta^{'}\rho\omega^2 + 2\rho_m(1-F_b)\sigma_{\omega 2}\frac{1}{\omega}\frac{\partial k_{tke}}{\partial x_j}\frac{\partial \omega}{\partial x_j}\end{aligned} \tag{5}$$

where k_{tke} is the kinetic energy of the turbulent fluid, ω is turbulence frequency , P_{kb} and $P_{\omega b}$ are the turbulent kinetic energy terms due to buoyancy, P is the kinetic energy term due to the velocity gradient, μ is the dynamic viscosity coefficient, and $\beta^{'}$、β、σ_k、σ_ω are constants. The specific expression for the mixing function F_b is

$$F_b = \tanh(\arg_1^4) \tag{6}$$

$$\arg_1 = \min[\max(\frac{\sqrt{k_{tke}}}{\beta^{'}\omega y}, \frac{500v}{y^2\omega}), \frac{4\rho\sigma_{\omega 2}k_{tke}}{CD_{k\omega}y^2}] \tag{7}$$

$$CD_{k_{tke}\omega} = \max(2\rho\sigma_{\omega 2}\frac{1}{\omega}\frac{\partial k_{tke}}{\partial x_j}\frac{\partial \omega}{\partial x_j}, 10^{-20}) \tag{8}$$

In Eq. (7), v is the viscosity coefficient of the fluid, $v = \frac{\mu}{\rho}$; $CD_{k_{tke}\omega}$ is a cross-diffusion term; and y is the minimum distance between the node and the wall. An expression for μ is

$$\mu = \frac{\rho a k_{tke}}{\max(a\omega, SF_2)} \tag{9}$$

where S is a fixed measure of shear strain rate,

$S = \sqrt{2W_{ij}W_{ij}}$, and $F_2 = \tanh(\arg_2^2)$

and where

$$W_{ij} = \frac{1}{2}\left(\frac{\partial u_i}{\partial x_j} - \frac{\partial u_j}{\partial x_i}\right) \tag{10}$$

$$\arg_2 = \max(\frac{2\sqrt{k_{tke}}}{\beta^{'}\omega y}, \frac{500v}{y^2\omega}) \tag{11}$$

2.1.3 Cavitation Model

In this study, the Schnerr-Sauer cavitation model (Schnerr 2001) is used to analyze the cavitation problem. The evaporation rate R_e and the condensation rate R_c of the model are expressed as

$$R_e = \frac{\rho_v\rho_w}{\rho_m}\alpha(1-\alpha)\frac{3}{R_B}\sqrt{\frac{2}{3}\frac{p_v - p}{\rho_w}} \tag{12}$$

$$R_c = \frac{\rho_v\rho_w}{\rho_m}\alpha(1-\alpha)\frac{3}{R_B}\sqrt{\frac{2}{3}\frac{p - p_v}{\rho_w}} \tag{13}$$

where R_B, the bubble radius, is given by

$$R_B = (\frac{\alpha}{1-\alpha}\frac{3}{4\pi}\frac{1}{N})^{\frac{1}{3}} \tag{14}$$

and where α is the volume fraction of steam and N is the number of cavitations per unit volume. The governing

equation is

$$\frac{\partial \varphi_v}{\partial t}+\frac{\partial}{\partial x_i}(\varphi_v u_i)=Fva\frac{2\alpha_{ncg}(1-\varphi_v)\rho_v}{R_B}\sqrt{\frac{2}{3}\frac{P_V-P}{\rho w}} -Fcon\frac{3\varphi_v\rho_v}{R_B}\sqrt{\frac{2}{3}\frac{P-P_V}{\rho w}} \tag{15}$$

In this equation, $F_{va}=50$ and $F_{con}=0.001$ are empirical constants taken from published work (Meng et al. 2019); P_v is the pressure of the water vapor; $\rho_v, \rho w$ are, respectively, the densities of water vapor and water; $\alpha_{ncg}=5\times10^{-4}$ is the volume fraction of non-coagulate gas; and $R_B=1\times10^{-6}$ m is the gas nucleus radial reference from the Rayleigh formula.

2.1.4 Six-Degrees-of-Freedom Model and UDF

UDF (user-defined functions) is a secondary development program based on C language that can be dynamically loaded into Fluent19.0. There are two loading methods for UDF: interpreted and compiled. Interpretation does not need to compile. It can be directly loaded and is very simple to use, although its calculations are slow. It needs to be compiled using the compiled software before it can be used. Its calculation speed is then fast, making the running time short. Considering the number of grids and the complexity of programming, this study uses compiled loading for UDF. At the same time, the fluid force and moment of the underwater projectile need to be output, which adds to the analytic efficiency and greatly improves the calculated results. The 6DOF solver of FLUENT software is used in all cases to solve for the motion of a underwater projectile. According to the force balance of the projectile, the displacement, velocity, and other variables of the projectile are calculated, to determine the position of the projectile's center of mass and the direction of its motion. The center of mass of the projectile and the direction of motion obtained in calculation step *n* can be used to calculate these quantities in calculation step (*n* + 1). The equations are

$$\overrightarrow{x_{c,g}^{n+1}}=\overrightarrow{x_{c,g}^{n}}+\overrightarrow{v_{c,g}}\Delta t \tag{16}$$

$$\overrightarrow{\theta_{c,g}^{n+1}}=\overrightarrow{\theta_{c,g}^{n}}+G\overrightarrow{\omega_{c,g}}\Delta t \tag{17}$$

where $\overrightarrow{v_{c,g}}$ (given below in Eq. (18)) is the linear velocity of the projectile, $\overrightarrow{\omega_{c,g}}$ is its angular velocity, $\overrightarrow{\theta_{c,g}^{n}}$ is calculation step *n* in the projectile's direction of motion, $\overrightarrow{x_{c,g}^{n}}$ is the position of the projectile's center of mass at the *n*th calculation step, and *G* is the transform matrix.

$$\overrightarrow{v_{c,g}}=\frac{v_0}{1+\alpha_c v_0 t} \tag{18}$$

In the formulation, v_0 is the initial velocity; α_c is the coefficient of velocity attenuation, and $\alpha_c=\rho_w A_0 C_d/2m_p$, where m_p is the mass of the projectile.

2.2 Computation model and Domain

In this study, a flat headed conical projectile made of tungsten alloy with a diameter of 5.8 mm was used as a model. In order to study the characteristics of the projectile entering water at different velocities, the study got better accuracy by calculating less. In this study, a three-dimensional model is used to numerically calculate four identical projectiles entering vertically, with different entry velocities (Hao, 2022).

The head of the main underwater projectile used in this study is a 16.5-mm truncated cone, the projectile head diameter is 2.6 mm, the head shape is conical flat-head. Its overall length is 30 mm. The conical flat-head projectile enters the water vertically at 300, 400, 500 and 600m/s respectively The cavity development, ballistic shape, and hydrodynamics of the projectile at different speeds were studied. In this study, SolidWorks was used for geometric modeling, followed by meshing of the model using ICEM CFD 19.0. The resulting grid was then imported into Fluent 19.0 for calculation, and the calculation results were analyzed using CFD-post. Finally, the analysis data was imported into Origin for plotting.

Figure 1 is the global sketch of the grid and the local sketch of the projectile surface. Figure 2 shows three different numbers of grids 1.3×10^6, 2×10^6 and 3×10^6. The velocity of the projectile is 400m / s. It can be seen that the velocity of the 1.3×10^6 grid attenuates faster, and the attenuation speed of 2×10^6 and 3×10^6 is not much different. This paper chooses the number of 2×10^6 grids for research. The y+ values is approximately 1.(see,Fig3)

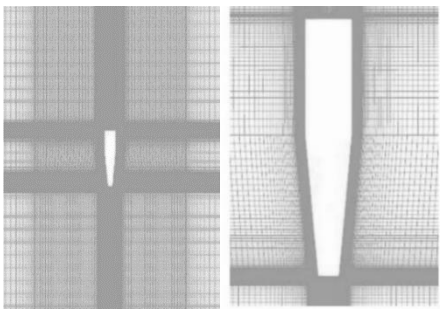

(a) (b)

Fig. 1 Grid diagrams, (a)Global Grid (b)Local Grid

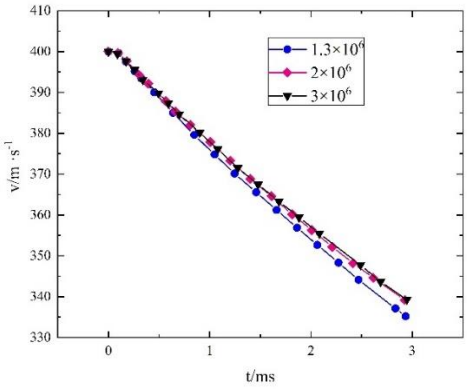

Fig. 2 Speed vs, time to verify mesh independence

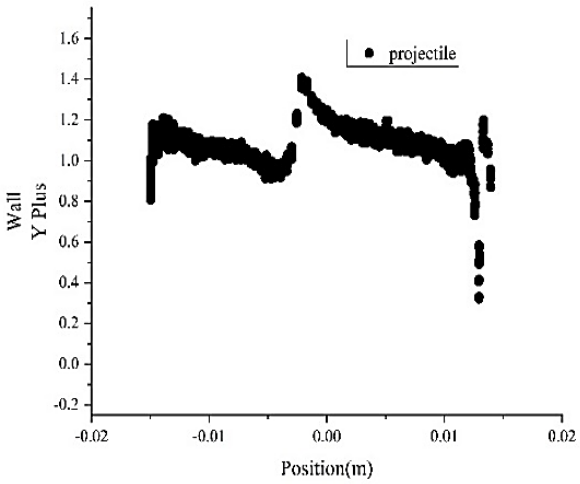

Fig. 3 Y plus diagram of projectile

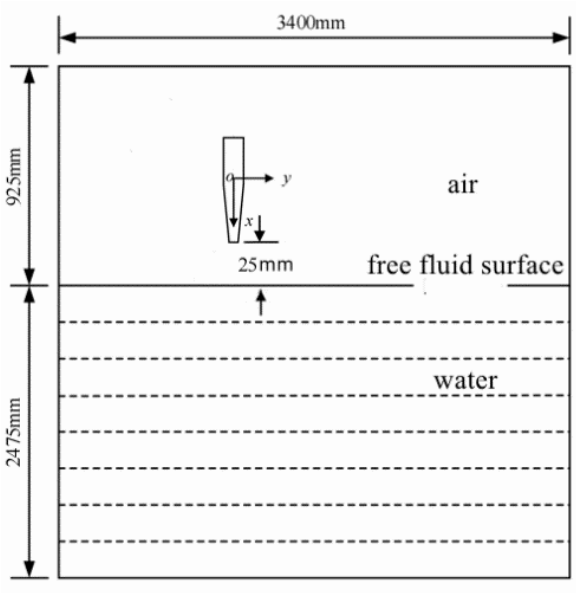

Fig. 4 Computational domain

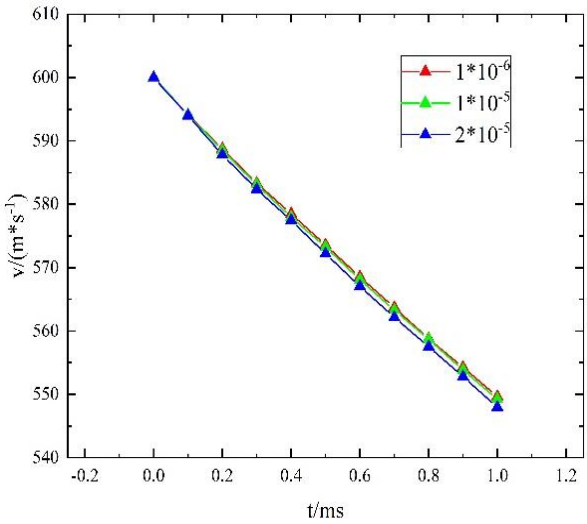

Fig. 5 Time steps independency

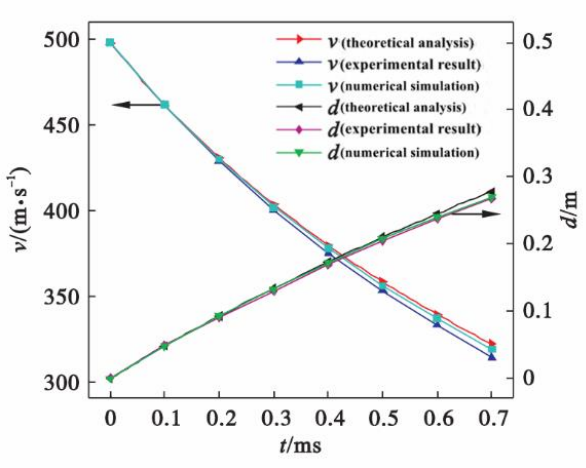

Fig. 6 Speed vs. time to validate the calculational method

Fig. 4 shows the computational domain of the numerical simulation method, in which the *z* value is set equal to zero; the cylindrical computational domain is a square with side length of 3400mm; the vertical range of the air part is 925 mm and the liquid depth is 2475 mm. The coordinate origin of the projectile is shown in the figure. The initial distance between the front end of the projectile and the water surface is 25 mm. Gravity acts in the *x* direction. The surface of the projectile is the wall condition, and the edge of the computational domain is the computational boundary. A hexahedron structure network is used for grid setting and refinement to ensure the accuracy of the model.

2.3 Numerical Methods and Verification

In this study, using the finite volume method, discrete equations are established for following the fluid motion in time and space. The PRESTO scheme is used for the spatial dispersion of the pressure field, and the gradient solution of the equation is determined by the least-squares method. The dissipation, turbulence, and momentum equations in the model equations are all second-order upwind forms. Dynamic mesh technology is used to update the mesh, and the process of high-speed projectiles entering water vertically is simulated numerically. The time step Δt is 1×10^{-5}s , and the number of max iterations is 20 (Wang 2016)

$$\Delta t = \frac{\text{Courant} * \Delta x}{\overrightarrow{v_{c,g}}} \tag{19}$$

Where Δx is overall length of projectile, the value of Courant is an empirical constant that typically falls within the range of 0.2 to 0.01 in order to maintain the accuracy of the calculation. The velocity attenuation remains consistent when the time step is either 1×10^{-5} or 1×10^{-6}. The velocity attenuation is more rapid with a time step of 2×10^{-5}s., as illustrated in Fig 5.

In order to check the correctness of the research method, the vertical water entry of a flat-nosed projectile model in the work of Guo (Guo 2012) is simulated numerically. The overall length of the projectile used in that study was 38.1 mm and its diameter was 12.65 mm.

Its initial velocity was 498.1 m/s. The calculated results show that the velocity attenuation and water entry depth of the projectile are consistent with Guo's experimental results, as shown in Fig. 6. These experiments support the correctness of the numerical calculation method in this paper.

3. NUMERICAL CALCULATIONS AND RESULTS

In this study, identical projectiles with initial velocities of 300, 400, 500, and 600 m/s were numerically simulated. By considering the mixing of water, water vapor, and air, the influence of velocity on the cavitation characteristics of projectiles entering water vertically was studied. By comprehensively analyzing the differences of underwater cavitation of high-speed projectiles at different speeds, and with different ballistic and fluid-mechanics characteristics, the underwater stability of projectiles at different speeds after entering the water was analyzed and judged.

The three graphs in Fig.7 show the instantaneous water-phase volume fraction produced by projectiles with four water-entry velocities at three different times after water entry. The cavitation behavior is similar for

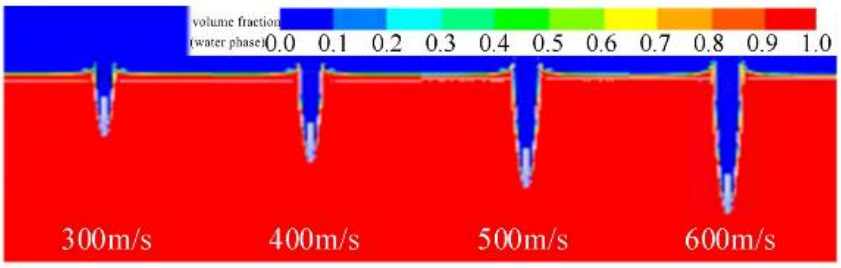

(a) t = 0.2 ms.

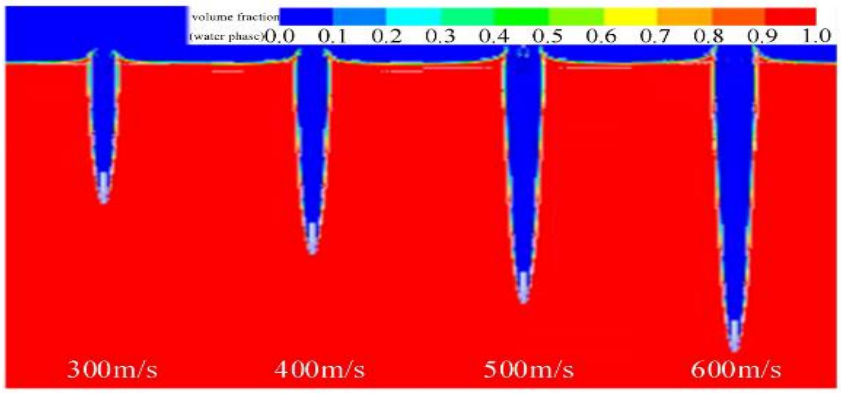

(b) t = 0.5 ms.

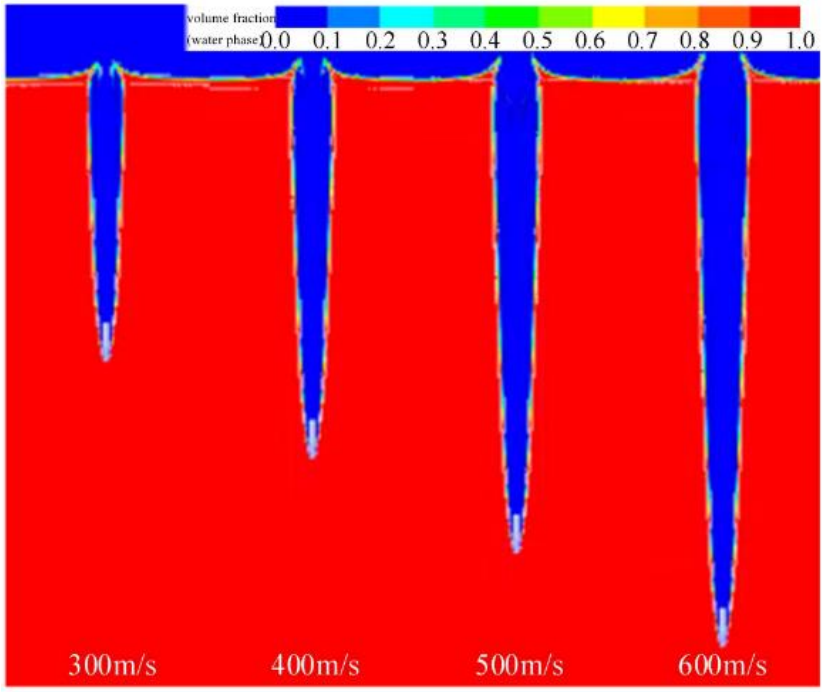

(c) t = 0.8 ms.

Fig. 7 Water phase volume fraction cloud diagrams for different water entry velocities

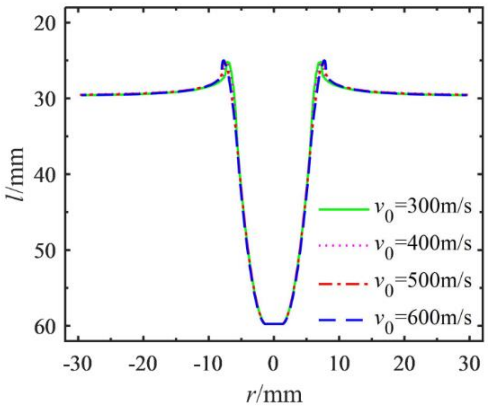

(a) Water Entry Depth 1*H*.

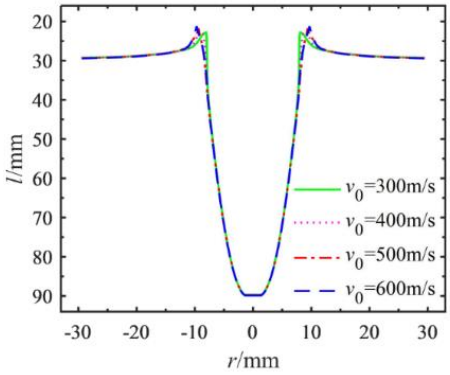

(b) Water Entry Depth 2*H*.

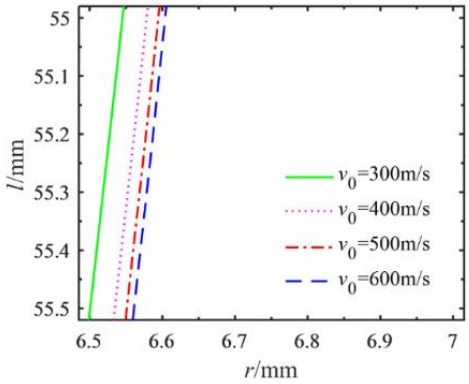

(c) Local amplification of right cavitation wall at water depth 2*H*.

Fig. 8 Cavitation shapes for different water entry speeds

projectiles with different velocities after water entry, including the trends of radial expansion, axial stretching, and surface closure of the cavitation. Yet, at the same time, the cavity development patterns of water entry at different speeds are distinctly different. In the first 0.2 ms, the top of the cavitation bubble is open to the air. The greater the velocity, the greater the length and diameter of the cavitation bubble (see Fig. 7(a)). When the time increases to 0.5 ms, the top of the cavitation bubble tends to move closer to the axis (see Fig. 7(b)). When the time reaches 0.8 ms, and the velocity is reduced, the degree of surface closure is greater, indicating, as one would expect, that lower speed leads preferentially to surface closure (see Fig.7(c)). With the passage of time, the larger the velocity of the projectile, the larger the cavity radius, which is consistent with the cavity state of the projectile with different velocities in different containers in Fan Chunyong 's study (Fan 2022). In addition, for the same time, with the water entry velocity of the projectile increases, the fluctuation range of the water surface around the head of the projectile will be greater, because the drag on the projectile increases with an increase of the velocity, which also makes the water gain greater kinetic energy.

Figure 8 shows cavitation shapes for projectiles with different velocities at different depths. The depths are 1*H* and 2*H*, where *H* is the length of the projectile. The lines in the figure outline the cavity. The comparative results show that for the same penetration depth the projectile with larger initial velocity has a larger diameter of projectile tail cavity, but the shape of the cavity at the head does not change as the velocity changes. From Figs.7 and.8, it can be seen that with the same water entry time, the cavitation length of the projectile increases with the increase of the velocity. When the water entry depth is the same, the cavity shape is basically the same, and the increase of the velocity has little effect on the cavitation diameter. This is consistent with the findings of Zitao Guo. That work showed that projectiles of the same shape have similar cavity sizes at different initial velocities (Guo 2020).

3.1 Analysis of Underwater Characteristics of Projectile

Figure 9 shows the dependence of velocity on time for various initial velocities of the projectile. Table 1 shows the underwater velocity attenuation rate of projectiles with different initial velocities. By comparing Fig. 9 and Table 1 it can be found that the attenuation per unit time increases as the initial velocity increases. Fig. 10 shows the projectile displacement as a function of time for the first 3 ms. When the velocity of the conical flat head projectile increases, the change of projectile displacement increases accordingly.

Figure 11 shows the drag coefficients of the projectiles as functions of time for various entry velocities for the first 3 ms. Figure 11(b) is an amplified section of the water entry impact stage, and Fig. 11(c) covers the time from 1.0 to 1.2 ms, a stable stage of cavitation flow. This study finds that the projectile drag coefficient

Table 1 Velocity attenuation rate of projectile for different water-entry velocities

Water-entry velocity/ m/s	Final velocity/m/s	Time/ms	Decay rate/% per ms
300	251.0	3	16.3
400	318.2	3	27.3
500	378.4	3	40.5
600	433.1	3	55.6

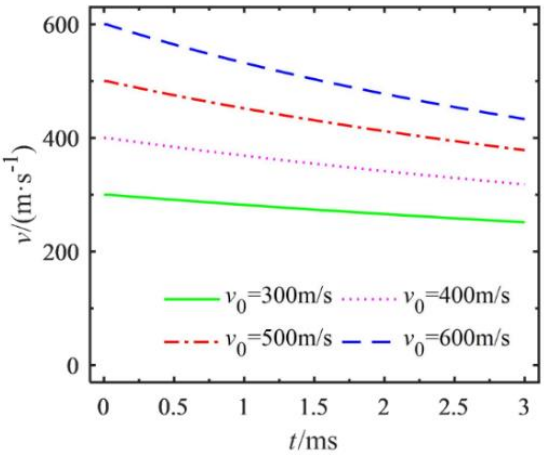

Fig. 9 Time dependence of projectile velocities

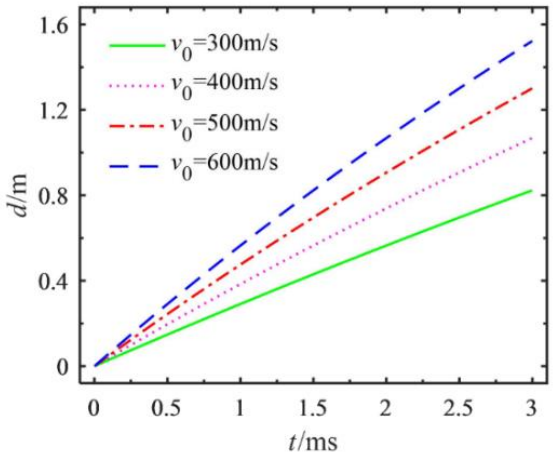

Fig. 10 Time dependence of projectile displacements

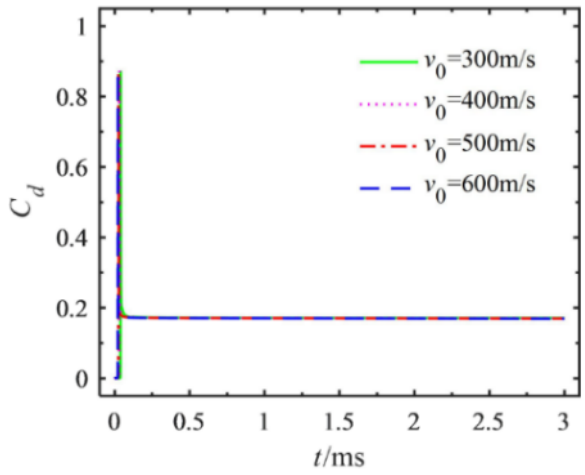

(a)

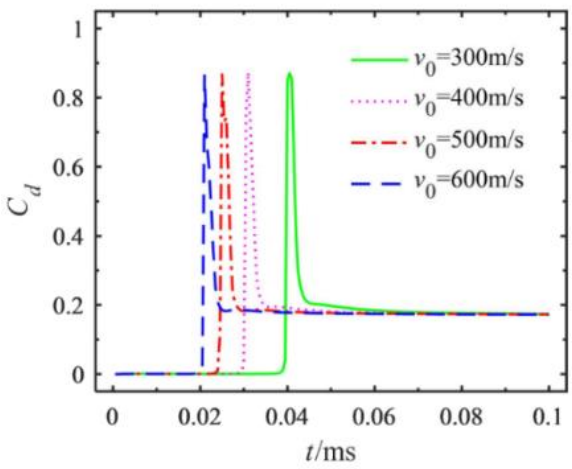

(b)

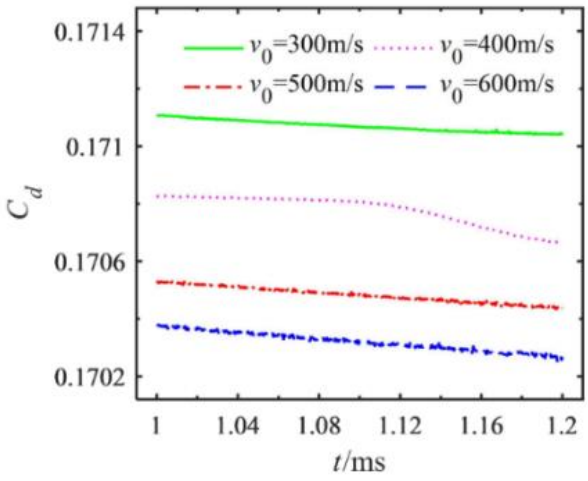

(c)

Fig. 11 Drag coefficient vs. time after water entry for several initial speeds.: (a) 0-3 ms. (b) 0-0.1 ms. (c) 1-1.2 ms

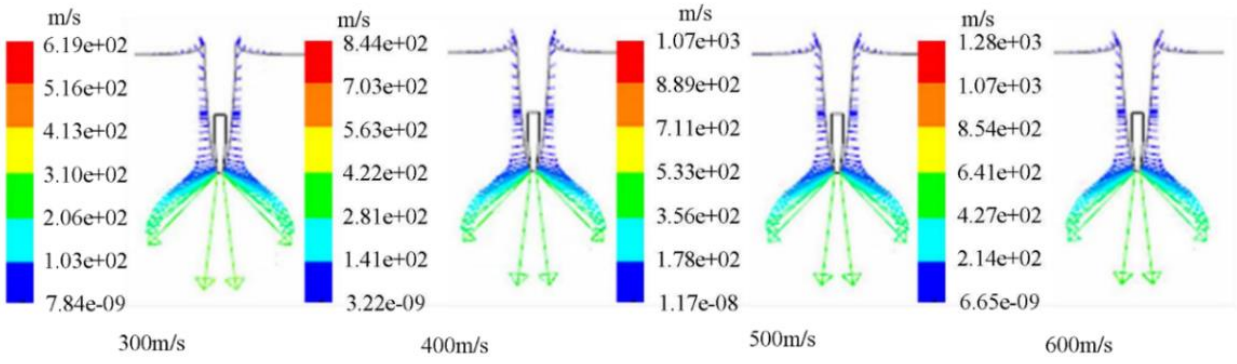

Fig. 12 Velocity vector diagrams of cavity wall at displacement 2*H* for several entry velocities

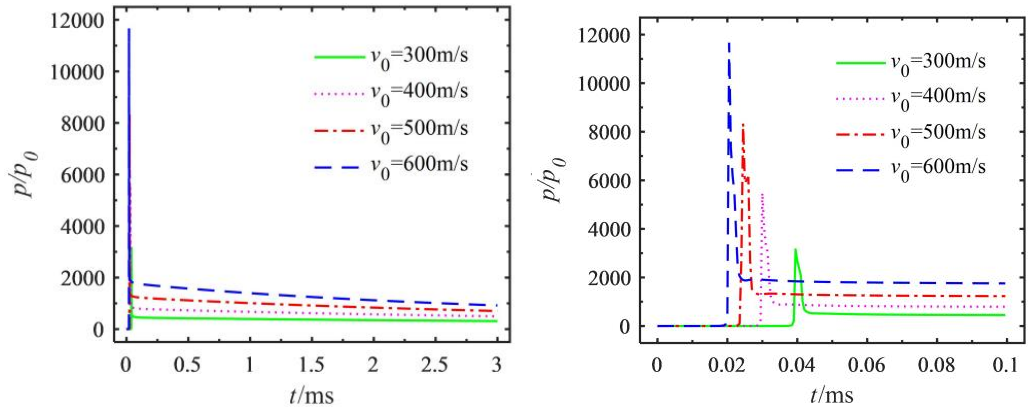

Fig. 13 Time dependence of maximum pressure at projectile head. (a) 0-3 ms. (b) 0-0.1 ms

changes only slightly as the velocity changes (see Fig. 11(a)). A very large drag coefficient peak is generated at the moment of water entry; it then decreases rapidly. The drag coefficient gradually decreases after the cavity flow becomes stable. It is clear from Fig. 11(b) that the peaks of the drag coefficients encountered by projectiles with different initial velocities entering water are similar to each other when they travel under water, but the greater the initial velocity, the earlier the drag coefficient reaches its peak after water entry. The higher the initial velocity, the smaller the drag coefficient, but with only small differences in its value (see Fig. 11(c)). It can be concluded that the initial velocity of water entry has very little effect on the drag coefficient of the conical flat head projectile, but the time for the projectile to reach the peak value decreases as the water entry velocity increases.

3.2 Analysis of underwater cavity flow fields of projectiles

Figure 12 shows the instantaneous bubble wall velocity vectors at a water entry depth 2*H* for projectiles with different initial velocities. After a projectile enters the water vertically, the cavity walls around it are expanded downward at a certain angle, and the closer to the position of the projectile head, the greater the inclination of the vacuole wall velocity vector and the greater the velocity. The expansion direction of the bubble wall is oblique at the top of the bubble. It can also be seen that the expansion velocity of the cavitation wall is very different for different initial velocities when the projectile is in the same position The faster the water entry velocity for conical flat head projectiles, the faster the expansion of the cavitation wall . In other work (Jafarian 2016), their findings are essentially the same as those of the present study.

Figure 13(a) shows the maximum pressure at the projectile head in the first 3 ms. An amplified view for the first 0.1 ms appears in Fig. 13(b). It can be seen that the maximum pressure change on the head has the same general trend for different velocities. When hitting the free surface, a sharp peak appears. After entering the flow stability stage, the maximum pressure decreases slowly. The greater the velocity of the same projectile, the faster it reaches the peak pressure after entering the water. (see Fig. 13(b)). After entering the flow stability stage, the pressure increases with the increase of velocity. the peak value can reach 11,600 times atmospheric pressure.

3.3 Underwater trajectory analysis of projectiles with different head shapes

To study the ballistic stability of projectiles with three head shapes entering water vertically, conical cone head and elliptical flat head projectiles with the same size and material as the conical flat head projectiles are studied.

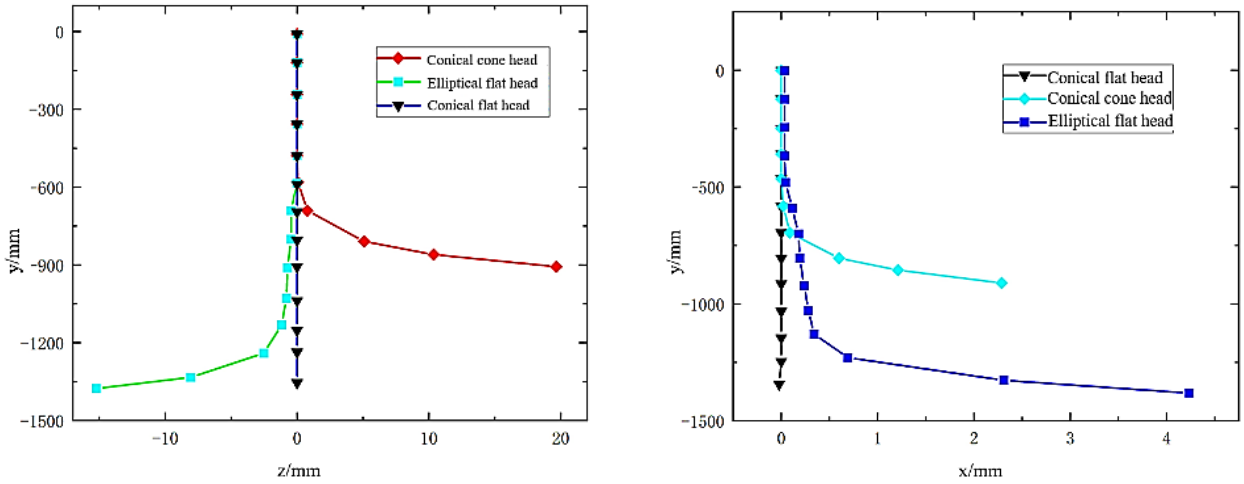

(a)*yz* plane trajectory projection. (b) *xy* plane trajectory projection.

Fig. 14 Trajectories of centroids of projectiles with different shapes

Before the projectile enters the water, its centroid trajectory is almost a straight line. After entering the water, the projectile trajectory begins to deviate. As the contact area between the projectile and the water increases, the projectile centroid begins to shift significantly.

From Figs 14(a) and (b), the velocity of the projectile is 0 except for the *y* direction before entering the water, although the projectile extends in these directions. When the head of the projectile is contact with the water, and the lateral force is generated by small disturbance of the water flow. With an increase of the water area, the *x* and *z* directions offset increase. When the projectile enters the water, due to differences in the shapes of the heads, the hydrodynamic forces on the projectile are different. As time increases, the conical flat head projectile continues vertically. The elliptical flat head and conical cone head projectiles deviate in the x and z directions. The elliptical flat head projectile is deflected in the x+ direction and z- direction, the conical cone head projectile is deflected in the x+ direction and z+ direction, and the conical flat head projectile is almost not deflected. Therefore, the underwater stability of the conical flat head projectile is very better than that of the elliptical flat head projectile, and the stability of the conical cone head projectile is poor.

Figure 15 shows the velocity changes in the coordinate directions during the process of projectiles vertical water entry with different shapes. The projectile velocity remains almost unchanged before contact with free liquid surface. From Figs.15 (a) and (c), the velocity components in the *x* and *z* directions are basically zero from 0-0.7 ms. After 0.7 ms, the projectile head contacts the water, resulting in fluid dynamics in the *x* and *z* directions. It can be seen from Fig. 15(b) that at the same time before the projectile enters the water, the speed in the *y* direction of the conical flat head is the smallest, and the velocity in the *y* direction of the conical cone head is the largest. This is because the weight of the projectile is nearly the same, the resistance of the conical flat head is larger, and the velocity decays faster. After 0.9 ms, the conical cone head shows poor stability. The centroid is deflected, and the contact area between the head of conical cone head projectile and the water in *y*-axis direction becomes larger, resulting in a larger fluid resistance in the *y*-axis direction and a very rapid speed attenuation.

5. CONCLUSION

In this study, through numerical simulation, the influence of velocity and head shape on the vertical water entry process of projectile is studied., and the ballistic characteristics, the flow fields, and the cavitation behaviors are revealed. The underwater stability of the projectiles is also considered. Here are the principal conclusions:

(1) With the water-entry velocity of the projectile is creasing, the more rapid the decay of the velocity and the greater the underwater displacement in a given time, also the greater the velocity attenuation per unit time and the greater the change of the centroid position of the projectile. However, there is no direct effect of the velocity of the projectile on the drag coefficient in the water.

(2) For greater water entry velocity, the attenuation rate of velocity is more.

(3)The pressure at the projectile's head peaks when it touches the water surface, then drops sharply, and finally levels off. In the stable stage of the flow, the greater the velocity, the greater the pressure on the projectile's head.

(4)After the flow is stable, the pressure increases with the increase of velocity.

(5) The stability of the projectile with conical flat head is the best, and the stability of the conical cone head projectile is the worst.

Based on the above results, the research team will further test the influence of the two tuning parameters of the cavitation model. The effects of different turbulence models and mesh shapes on numerical calculations will be studied, and the ballistic stability and cavitation characteristics of projectiles with different shapes and different angles of incidence will also be further studied.

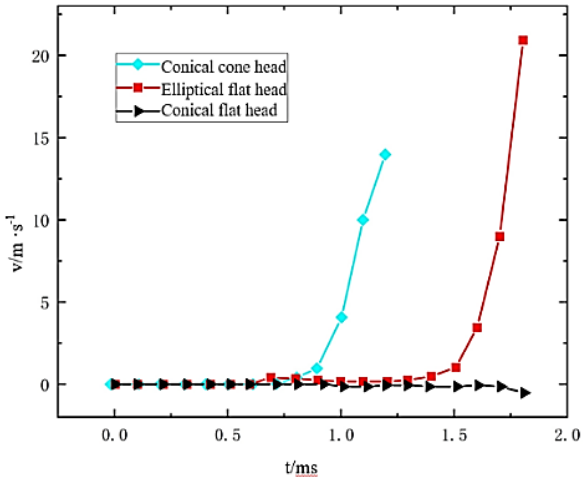

(a) Velocity in *x* direction.

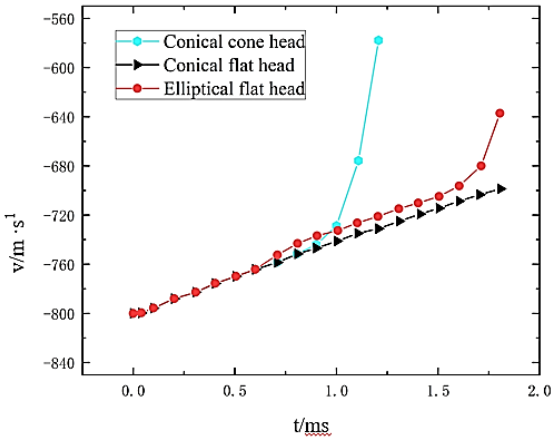

(b) Velocity in *y* direction.

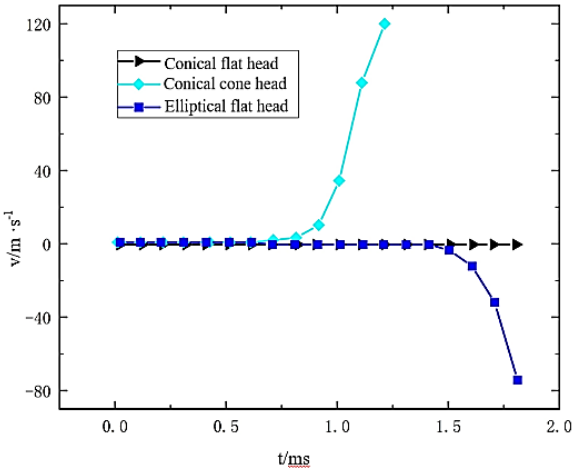

(c) Velocity in *z* direction

Fig. 15 Components of velocities of projectiles

CONFLICT OF INTEREST

The authors declare that they have no known competing financial interests or personal relationships that could have appeared to influence the work reported in this paper.

AUTHORS CONTRIBUTION

B. Hao guides and carries out the numerical simulation of this study; Y. G. Lu designs the simulation scheme and the writing of the paper; H. Dai prepares all the charts of this paper.

REFERENCES

Chen, S. R., Shi, Y., Pan, G., & Gao, S. (2021). Experimental research on cavitation evolution and movement characteristics of the projectile during vertical launching. *Journal of Marine Science and Engineering*, 9, 1359. https://doi.org/10.3390/jmse9121359

Fan, C. Y., Wang, M., & Li, H. (2022). High speed water entry phenomenon comparison of projectile with free and constant speed. *Journal of Applied Physics*, 132, 064701. https://doi.org/10.1063/5.0103515

Guo, Z. T., Chen, T., Mu, Z. C., & Zhang, W. (2020). An investigation into container constraint effects on the cavity characteristics due to high-speed projectile water entry. *Ocean Engineering*, 210 https://doi.org/10.1016/j.oceaneng.2020.107449

Guo, Z. T. (2012). China National Knowledge Infrastructure: Research on characteristics of projectile water entry and ballistic resistance of targets under different mediums, [Doctoral Dissertation, Harbin Institute of Technology], ProQuest Dissertations and Theses Global.

Guo, Z. T., Zhang, W., Wang, C. (2012). Experimental and theoretical study on the high-speed horizontal water entry behaviors of cylindrical proje- ctiles. *Journal of Hydrodynamics*, 24(2), 217-225. https://doi.org/10.1016/S1001-6058(11)60237-0

Hao, B., & Yang, B., Du, C. J., Dai, H., Lui, L. W. (2022) Influence rule of projectile density on the

characteristics of high-speed water-entry cavity. *Journal of Applied Fluid Mechanics*, 15(6), 1901-1912, https://doi.org/10.47176/jafm.15.06.1310

Huang, L. (2018). China National Knowledge Infrastructure: Research on variable medium motion simulation and ballistic characteristics of supercavitatinghigh-peed projectile, [Masteral Dissertation, North University of China], ProQuest Dissertations and Theses Global.

Jafarian, A., & Pishevar, A. (2016). Numerical simulation of steady supercavitating flows. *Journal of Applied Fluid Mechanics*, 9(6), 2981-2992. https://doi.org/10.29252/jafm.09.06.26209

Lee, M., Longoria, R. G., & Wilson, D. E. (1997). Cavity dynamics in high-speed water entry. *Physics of Fluids*, 9(03), 540-550. https://doi.org/10.1063/1.869472

Meng, Q. C., Yi, W. B., Hu, M. Y., Zhang, Z. H., Lui, J. B. (2019). Study on the form and hydrodynamic characteristics of vertical water entry cavitation of high speed projectile. *Chinese Shipbuilding*, 60(03), 12-2.

Miloh, T. (1981). Wave slam on a sphere penetrating a free surface. *Journal of Engineering Mathematics*, 15(3), 221-240. https://doi.org/10.1007/bf00042782.

Miloh, T, (1991a). On the initial-stage slamming of a rigid sphere in a vertical water entry. *Applied Ocean Research*, 13(1), 43-48. https://doi.org/10.1016/s0141-1187(05)80039-2

Miloh, T. (1991b). On the oblique water-entry problem of a rigid sphere. Journal of Engineerig Mathematics, 15(1), 77-9. https://doi.org/10.1007/BF00036603.

Schnerr, G. H., & Sauer, J. (2001, May-June). *Physical and numerical modeling of unsteady cavitation dynamics*. [Conference session], Fourth International Conference on Multiphase Flow New Orleans, LA, USA. https://doi.org/10.1016/S0032-5910(01)00496-X

Smirnov, N. N., Kiselev, A. B., & Zakharov, P. P. (2020). Numerical simulation of the hypervelocity impact of the ball and the spherical containment in three-material statement， *Acta Astronautica* 171 215–22. https://doi.org/10.1016/j.actaastro.2020.03.010

Smirnov, N. N., Kiselev, A. B., Zakharov, P. P., Muratov, R. V., & Bukharinskaya, D. M. (2022). The usage of adaptive mesh refinement in simulation of high-velocity collision between impactor and thin-walled containment. *Acta Astronautica*, 194, 401–410. https://doi.org/10.1016/j.actaastro.2021.12.017

Wang, Y. W., Huang, C. G., Fang, X., Wu, X. C., Du, T. Z. (2016). On the internal collapse phenomenon at the closure of cavitationbubbles in a deceleration process of underwater vertical launching. *Applied Ocean Research*, 56, 157-165 . https://doi.org/10.1016/j.apor.2016.02.001

Wang, X. Y. (2019). China National Knowledge Infrastructure: Numerical study on vertical rotating water entry process of small rotating body, [Masteral Dissertation, Harbin Institute of Technology], ProQuest Dissertations and Theses Global.

Xiao, H. Y., Luo, S, Zhu, Z., Yu, Y., (2019). Small angle water entry ballistic characteristics of high-speed projectile. *Journal of Beijing Institute of Technology*, 39(08), 784-791. https://doi.org/10.15918.08.003